

Dual-Terahertz-Comb Spectrometer on CMOS for Rapid, Wide-Range Gas Detection With Absolute Specificity

Cheng Wang[✉], Student Member, IEEE, and Ruonan Han, Member, IEEE

Abstract—This paper describes the design and implementation of a 220–320 GHz spectrometer consisting of a pair of 65-nm CMOS chips. The spectrometer utilizes two counter-propagating frequency-comb signals to seamlessly scan the broadband spectrum and significantly reduces the total scanning time through high parallelism. The comb signal, with ten equally spaced frequency tones, is generated and detected by a chain of inter-locked transceivers on chip. The large reduction of required tuning range for each transceiver enables peak energy efficiency across a wide bandwidth. Each transceiver is based on a multi-functional electromagnetic structure, which serves as a frequency doubler, sub-harmonic mixer and an on-chip radiator simultaneously. In particular, theory and design methodology of a dual-transmission-line feedback scheme are presented, which maximizes the transistor gain near its cutoff frequency f_{\max} and enhances the harmonic generation efficiency. The spectrometer chip has a measured total radiated power of 5.2 mW and a measured single-sideband noise figure of $14.6 \sim 19.5$ dB, representing the highest generated power and sensitivity of silicon-based terahertz circuits. The chip consumes a dc power of 1.7 W. Finally, absorption spectrum of acetonitrile (CH_3CN) and carbonyl sulfide is obtained, which agree with the JPL spectroscopy catalog.

Index Terms—CMOS, frequency-comb, maximum power gain, molecular spectroscopy, slot line, terahertz (THz), transceiver.

I. INTRODUCTION

TERAHERTZ (THz) and millimeter waves can interact with polar molecules in the gas phase. Through the excitation of molecular rotational states, the wave energy is transferred to the molecules. The associated absorption spectrum in a frequency-scanning setup can, therefore, be used as a unique fingerprint for molecule identifications [1]. It is noteworthy that such rotational behavior is quantized and its spectrum exhibits periodicity in the frequency domain with a spacing determined by the moment of inertia [2]. For example, carbonyl sulfide (OCS) has spectral lines every ~ 12 GHz [3]. Due to such spectral redundancy, a 30-GHz bandwidth covers the absorption lines of any molecule with at least three

Manuscript received May 2, 2017; revised August 1, 2017; accepted September 8, 2017. Date of publication October 16, 2017; date of current version November 21, 2017. This paper was approved by Guest Editor Chih-Ming Hung. This work was supported in part by the National Science Foundation under Grant ECCS-1653100, in part by the MIT Center for Integrated Circuits and Systems, and in part by the Advanced Concepts Committee funding from MIT Lincoln Laboratories. (Corresponding author: Cheng Wang.)

The authors are with the Department of Electrical Engineering and Computer Science, Massachusetts Institute of Technology, Cambridge, MA 02139 USA (e-mail: wangch87@mit.edu).

Color versions of one or more of the figures in this paper are available online at <http://ieeexplore.ieee.org>.

Digital Object Identifier 10.1109/JSSC.2017.2755693

atoms heavier than boron [4], and a bandwidth of 100 GHz enables coverage of even lighter molecules such as hydrogen cyanide (HCN), which has lines every ~ 88 GHz [3]. Meanwhile, when the gas pressure is reduced below ~ 0.1 torr, the spectral linewidth is only limited by the Brownian motion of molecules (rather than inter-molecular collision), and decreases to ~ 1 MHz or below (see Section V) [1]. The resultant absolute specificity ($10^5 \sim 10^6$ quality factor Q of the spectral line), combined with the aforementioned wide detection range of molecules, makes a THz spectrometer a very powerful tool for chemical gas sensing.

With the recent progress in silicon-based THz integrated circuits, there is a growing interest in building chip-scale THz spectrometers [5], [6]. Such efforts are divided into two categories: a narrow-pulse-based approach and a continuous-wave (CW) frequency-tuning approach. The former facilitates the generation of broadband signal [7]–[9], but has three critical problems: 1) due to the ultra-low duty cycle of signal gating, large bandwidth (i.e., short pulse) leads to small average radiation power and very long signal integration time; 2) only homodyne detection, which is a few orders of magnitude less sensitive than heterodyne detection, can be used due to the lack of phase coherency between the pulse source and detector; and 3) interferometry with Fourier transform is needed to resolve the frequency components of a broadband pulse. However, the optical path difference required for a 10-kHz resolution is 30 km, which is impractical. In [10], the spectrometer based on electromagnetic scattering is an alternative to interferometer, but its resolution is still insufficient for the absolute-specificity requirement in rotational spectroscopy.

The CW frequency-tuning approach, although not having the above problems, suffers from a significant tradeoff between bandwidth and performance. All circuits operating in the millimeter-wave frequencies rely on resonance with high quality factor (Q) to achieve minimum loss and maximum efficiency. As a result, it poses a fundamental limit between the achievable bandwidth and efficiency. In the THz range, this problem is even more severe, because on-chip tunable devices (e.g., MOS varactor) exhibit excessive loss, and optimum operation conditions (e.g., for maximum power gain) for transistors running near f_{\max} vary significantly from one frequency point to another, further reducing the bandwidth. In [11], a 245-GHz spectrometer generates 4-mW radiated power but only has 14-GHz bandwidth. In [12] and [13], broader bandwidths are achieved at the expense of degraded radiated power (0.1 mW) and noise figure (NF) (18.4–23.5 dB when the antenna beam collimation factor is de-embedded).

In addition, given a typical 10-kHz resolution and 1-ms integration time, scanning a 100-GHz bandwidth with a single tone requires as long as 3 h.

In this paper, we describe a rapid and energy-efficient spectrometer ($\text{Tx} + \text{Rx}$) that is implemented in a 65-nm bulk CMOS process ($f_{\max} = 250$ GHz) [14]. Based on a bi-directional, dual-frequency-comb architecture, our spectrometer simultaneously uses 20 signal tones to achieve a seamless coverage of a 220–320 GHz band. The circuit consists of an array of active molecular probe (AMP) transceivers, which utilize multi-functional electromagnetic structures to maximize transistor performance with minimum overhead on the area and significant reduction in loss. Back-side radiation from on-chip antenna is adopted with the assistance of a hemispheric silicon lens attached at the bottom of the chip. The measured total radiated power of our spectrometer in the free space is 5.2 mW. The measured single-sideband NF (SSB NF), including the antenna loss, is 14.6–19.5 dB. To the best of our knowledge, these achieved generated power and detection sensitivity are the records in THz silicon chips. Its dc power consumption is 1.7 W, corresponding to a dc-to-THz radiated power efficiency of 0.3% or 1.8%, including or excluding the power consumption of circuitries between AMP stages, respectively. More profoundly, this paper showcases a new way of using parallelism in THz spectral scanning to break the traditional bandwidth-performance tradeoff.

This paper is organized as follows: in Section II, the architecture of the chip and the principle of the dual-frequency-comb spectroscopy are described. The design details of the AMP transceiver unit and other circuit blocks are given in Sections III and IV, respectively. In Section V, experimental characterization of the chip, as well as a THz spectroscopy demonstration for gas sensing, is presented. Finally, a conclusion with a performance comparison with other state-of-the-arts is given in Section VI.

II. OVERVIEW OF THE CMOS THZ SPECTROMETER

A. Dual-Frequency-Comb, Bi-Directional Spectroscopy

Compared with the conventional single-tone spectral-scanning scheme [Fig. 1(a)], the presented dual-frequency-comb architecture [Fig. 1(b)] channelizes the detection band by two identical frequency-comb chips with a 950-MHz frequency offset f_{IF} between their output radiation spectra. Each chip works under Tx and Rx modes simultaneously. From Chip A, ten equally spaced comb lines with 10-GHz frequency interval are transmitted through the gas sample and coupled into Chip B through on-chip antennas. Meanwhile, inside Chip A, the above ten comb lines are also used as local-oscillator (LO) signals for the heterodyne mixing of another ten comb lines radiated from Chip B. Finally, the 10×2 down-converted output signals at f_{IF} , which carry absorption spectral information of the gas, are extracted from the two chips. To fully cover the 100-GHz bandwidth, the spectra of the comb pair only need to sweep by 10 GHz. Finally, it is noteworthy that similar channelized transceiver schemes were also explored previously in impulse-radio ultra-wideband communications for pulse shaping and spectral efficiency improvement [15], [16].

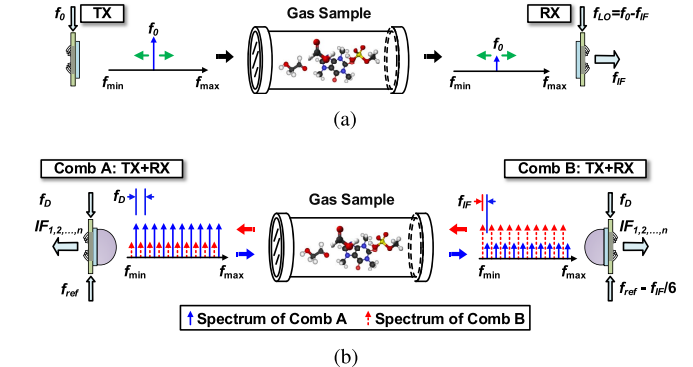


Fig. 1. Comparison between (a) conventional single-tone spectrometer and (b) proposed dual-frequency-comb, bilateral spectrometer chipset.

B. Chip Architecture

A block diagram of the spectrometer is given in Fig. 2(a). Under the Tx mode, the chip is driven by a tunable single-tone input signal, f_{ref} (45 ~ 46.67 GHz), which is then tripled to 135 ~ 140 GHz and power divided into up- and down-conversion chains. Through a series of cascaded SSB mixers, the chains produce signal tones, which are evenly spaced every 5 GHz. The 5-GHz frequency spacing is defined by a frequency divider ($\div 2$) with an external 10-GHz clock input, f_D . Each single-tone signal is then doubled by an active-molecular-probe (AMP) unit. Subsequently, the ten comb lines located at $6f_{ref} + i \cdot 10$ GHz ($i = -5$ to $+4$) are simultaneously radiated by on-chip antennas built in the AMPs through a hemispheric silicon lens [Fig. 2(b)] attached at the backside of the chip. The lens suppresses the substrate mode and reduces reflection at its silicon-air interface. Finally, in the far field, the frequency-comb signal is achieved by the spatial combining of all radiation tones. Under the Rx mode, the incident wave is coupled into the chip through the same reciprocal mechanism. Sub-harmonic mixing is performed also in each AMP, of which the driving signal behaves as LO. Compared with prior optical combs, which are based on mode-locked laser pulse [17], [18], our CW-type electronic comb offers excellent tuning capability, phase coherency (hence heterodyne detection), and high-frequency resolution. This architecture also enables scalability to higher bandwidth through extended cascading of AMP channels.

C. Advantages in Spectral-Scanning Efficiency and Speed

First, our spectroscopy scheme breaks the bandwidth-efficiency tradeoff in conventional RF-THz design (explained in Section I). By partitioning the overall spectrum, the required tuning range for each channel is reduced below 4.5%, which allows for high- Q topology (e.g., the feedback-induced AMP circuit to be presented in Section III) and keeps peak achievable performance across a broad frequency range. We will also show in Section III that the simultaneous transmit and receive scheme enabled in our THz front ends further reduces the power consumption by $\sim 2\times$.

Second, it is noteworthy that the spectral-scanning speed (i.e., integration time per data point needed for certain SNR) of a single-tone spectrometer with certain sensitivity is determined by the probing signal power, which is funda-

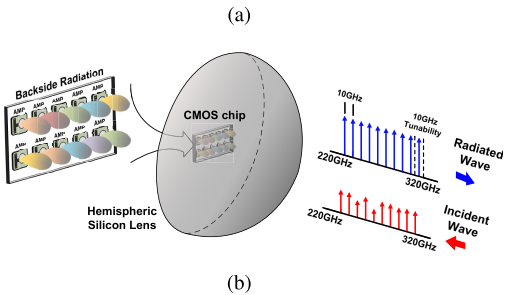
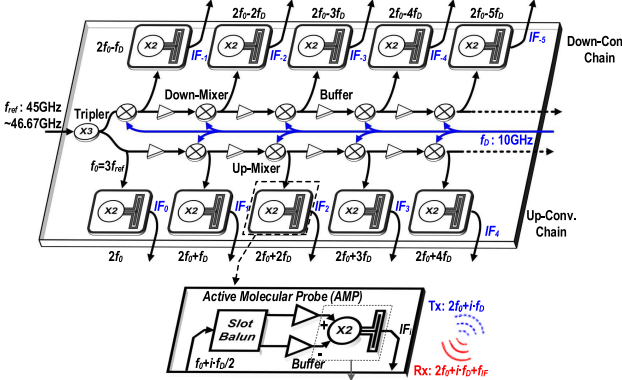


Fig. 2. (a) Circuit architecture of the CMOS spectrometer and each active molecular probe (AMP). (b) Backside radiation through a hemispheric silicon lens.

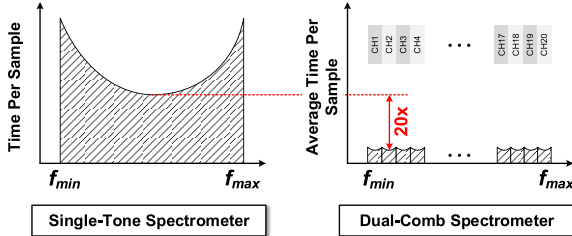


Fig. 3. Comparison of broadband spectral-scanning speeds between the conventional single-tone scheme and our dual-comb scheme. The total time needed is the size of the shaded area.

mentally limited by the population saturation of molecular rotational states [2]. In comparison, in a comb, each probing channel can reach such maximum speed, leading to a much shorter total scanning time through parallel operation. If the performance degradation of the single-tone scheme at the band edges is also taken into consideration, as shown in Fig. 3, the overall speed improvement factor in our comb is even much greater than the number of comb lines.

III. DESIGN OF ACTIVE MOLECULAR PROBE

The core of the active molecular probe (AMP), as shown in Fig. 2(a), is driven differentially by a fundamental signal f_0 , which is generated by the up-/down-conversion chains. As shown in Fig. 4, the AMP core serves as a radiating frequency doubler as well as a sub-harmonic mixer. In this section, it is shown that by using a multi-functional electromagnetic structure with a device embedding network, the frequency doubling, radiation coupling, and heterodyne detection are simultaneously achieved.

A. Odd-Mode Operation at the Fundamental Frequency f_0

At the fundamental frequency f_0 , propagation of the odd-mode signal inside the AMP is shown in Fig. 5(a). The

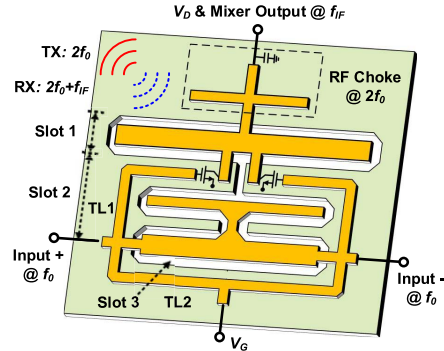


Fig. 4. 3-D view of the core of the active molecular probe (AMP).

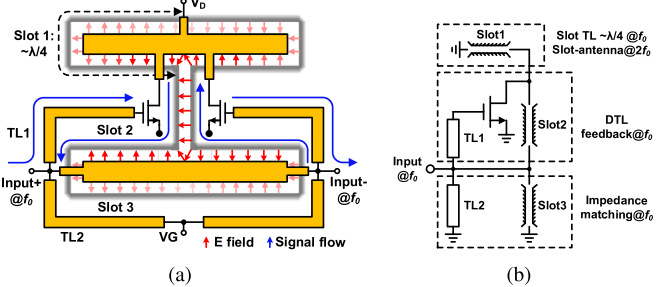


Fig. 5. (a) Odd-mode signal flow of the AMP at the fundamental frequency f_0 . (b) Schematic of the equivalent half circuit.

input signal is injected into the gates of NMOS transistor through shielded microstrip transmission lines TL_1 . The amplified signal from the device drains is then fed into a pair of near-quarter-wave slots (*Slot 1*) via two short microstrip lines. The simulated guided wavelength of slot 1 under TE mode is shown in Fig. 6. The coupling between the microstrip line and the slot happens, because the two conductors of the microstrip line (signal trace and ground plane) are physically connected to the two conductors of the slot (shown in Fig. 4). The high impedance presented by *Slot 1* leads to large voltage swing at the device drain terminals and enhances the device nonlinearity for harmonic generation. The input matching is performed by *Slot 3* and TL_2 .

An essential part of the AMP core is *Slot 2*, which serves as a feedback path and partially recycles the power generated by the drain back to the input. Due to the odd-mode operation at f_0 , the signal is allowed to propagate in the vertical part of *Slot 2* in the form of TE wave [19]. This can be visualized by the simulated field distribution of AMP at f_0 in Fig. 7(a). In Section III-B, detailed theoretical analysis is given on the design of the feedback path to reach the upper limit of transistor power gain, which is critical to conversion efficiency in the frequency-doubler mode of AMP. To facilitate this analysis, the AMP circuit at f_0 is translated into a half-circuit equivalence [shown in Fig. 5(b)]. It is obtained based on the symmetry of the circuit, where the central vertical line of the structure can be considered as virtual ground.

B. Double-Transmission-Line Feedback for Maximum Power Gain (G_{ma}) at f_0

In order to improve the harmonic generation efficiency, the transistor power gain should be maximized in order to reduce the input signal power. Meanwhile, the device

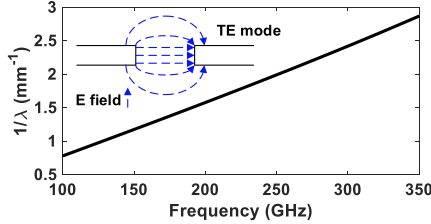


Fig. 6. Simulated guided wavelength of *Slot 1* at various frequencies.

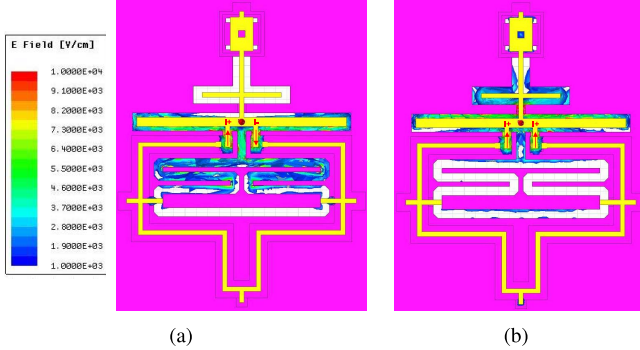


Fig. 7. Simulated electrical-field distribution of the AMP at (a) $f_0 = 137.5$ GHz with differential mode signal on the drain connectors and (b) $f_0 = 275$ GHz with common-mode signal on the drain connectors.

should remain unconditionally stable in order to avoid self-oscillation. For a two-port linear network (e.g., a transistor or a transistor with embedding network), which is modeled by its Y -parameters

$$[Y_0] = \begin{bmatrix} y_{11} & y_{12} \\ y_{21} & y_{22} \end{bmatrix} \quad (1)$$

the power gain G_{ma} obtained through only input and output conjugate matching is not the maximum achievable gain of the device. In [20], the following relationship:

$$\sqrt{\frac{G_{\text{ma}}}{U}} = \left| \frac{A - G_{\text{ma}}}{A - 1} \right| \quad (2)$$

is discovered between G_{ma} , the unilateral gain U , and A defined as

$$A = \frac{y_{21}}{y_{12}}. \quad (3)$$

Note that U is invariant if a lossless network is built around the transistor. This, however, changes A and, therefore, leads to different values of G_{ma} according to (2). Thus, an optimum transistor embedding network can be introduced to achieve the maximize possible value of G_{ma} . According to (2), when the new A is real and equals to

$$A_{\text{opt}} = -G_{\text{max}} = (1 - 2U) - 2\sqrt{U(U - 1)} \quad (4)$$

the maximum gain G_{max} , expressed as

$$G_{\text{max}} = (2U - 1) + 2\sqrt{U(U - 1)} \quad (5)$$

is obtained [21], which is close to $4U$, if $U \gg 1$.

In this paper, we present a double-transmission-line (DTL) feedback structure (Fig. 8) for gain boosting of AMP at fundamental frequency. Compared with the previous gain-boosting techniques using Y - Z embedding [20], neutralization [21], and an inductor/T-line/inductor embedding network [22], our

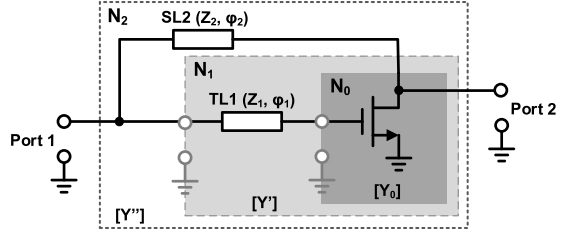


Fig. 8. Anatomy of transistor embedding network using DTL feedback.

scheme eliminates not only the lossy RF choke at the source (needed in [20] and [21]), but also the lumped-model inductors (used in [20] and [22]), which in practice exhibit significant distributed effects at THz. More importantly, by adopting a slot line as one of the feedback transmission lines, our scheme provides input–output harmonic isolation, which greatly enhances the harmonic generation efficiency (to be explained in Section III-C). Meanwhile, an analytical solution is derived that directly calculates the network parameters (i.e., Z_1 , φ_1 , Z_2 , and φ_2) needed to accurately achieve any power gain G_{ma} value from 0 to G_{max} , which was not presented in prior works. First, the real value of the new A''^1 associated with a given G_{ma} , according to (2), can be expressed as

$$A'' = \frac{y_{21}''}{y_{12}''} = \frac{G_{\text{ma}}\sqrt{U} - \sqrt{G_{\text{ma}}}}{\sqrt{U} - \sqrt{G_{\text{ma}}}}. \quad (6)$$

Then, we derive parameters of the MOSFET-TL1 cascading combination (N_1 in Fig. 8). The ABCD-parameter of the MOSFET is [23]

$$\begin{bmatrix} A_0 & B_0 \\ C_0 & D_0 \end{bmatrix} = \begin{bmatrix} -\frac{y_{22}}{y_{21}} & -\frac{1}{y_{21}} \\ \frac{y_{21}y_{12} - y_{11}y_{22}}{y_{21}} & -\frac{y_{11}}{y_{21}} \end{bmatrix}. \quad (7)$$

In addition, the ABCD-parameter of TL1 is

$$\begin{bmatrix} A_1 & B_1 \\ C_1 & D_1 \end{bmatrix} = \begin{bmatrix} \cos \varphi_1 & j Z_1 \sin \varphi_1 \\ \frac{j}{Z_1} \sin \varphi_1 & \cos \varphi_1 \end{bmatrix} \quad (8)$$

where Z_1 and φ_1 are the characteristic impedance and electrical length of TL1, respectively. Then, the ABCD-parameter of Network N_1 is derived as the product of the above two matrices

$$\begin{bmatrix} A_{10} & B_{10} \\ C_{10} & D_{10} \end{bmatrix} = \begin{bmatrix} A_1 & B_1 \\ C_1 & D_1 \end{bmatrix} \cdot \begin{bmatrix} A_0 & B_0 \\ C_0 & D_0 \end{bmatrix}. \quad (9)$$

From (9), the elements in the Y -parameter matrix of Network N_1 (denoted as $[Y']$ in Fig. 8) are expressed as

$$\begin{aligned} y'_{11} &= \frac{\frac{j}{Z_1} \sin \varphi_1 + \cos \varphi_1 \cdot y_{11}}{\cos \varphi_2 + j Z_1 \sin \varphi_1 \cdot y_{11}} \\ y'_{12} &= \frac{y_{12}}{\cos \varphi_1 + j Z_1 \sin \varphi_1 \cdot y_{11}} \\ y'_{21} &= \frac{y_{21}}{\cos \varphi_1 + j Z_1 \sin \varphi_1 \cdot y_{11}} \end{aligned}$$

¹As the gain plane representation given in [20] and Fig. 9 shows, although a certain G_{ma} is related to a set of complex values for A , the only real value of A achieves the highest stability factor K .

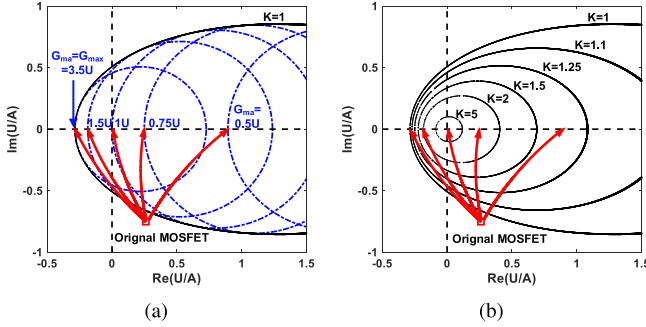


Fig. 9. Simulated U/A movement with DTL feedback on gain plane with (a) constant G_{ma} contour and (b) constant K contour.

$$y'_{22} = y_{22} - \frac{j Z_2 \cdot \sin \varphi_1 \cdot y_{21} y_{12}}{\cos \varphi_1 + j Z_1 \sin \varphi_1 \cdot y_{11}}. \quad (10)$$

Next, the second transmission line $SL2$ (realized by *Slot 2* in the AMP) is included. Its Y -parameter is expressed as

$$[Y_{SL2}] = \frac{1}{Z_2 \sin \varphi_2} \begin{bmatrix} -\cos \varphi_2 & 1 \\ 1 & -\cos \varphi_2 \end{bmatrix} \quad (11)$$

where Z_2 and φ_2 are its characteristic impedance and electrical length, respectively. Since Network N_1 and $SL2$ are connected in shunt at the two ports, the Y -parameter matrix of the entire combined network N_2 is derived as the sum of (10) and (11)

$$[Y''] = [Y'] + [Y_{SL2}] = \begin{bmatrix} y''_{11} & y''_{12} \\ y''_{21} & y''_{22} \end{bmatrix} \quad (12)$$

where

$$\begin{aligned} y''_{11} &= \frac{\frac{j}{Z_1} \sin \varphi_1 + \cos \varphi_1 \cdot y_{11}}{\cos \varphi_2 + j Z_1 \sin \varphi_1 \cdot y_{11}} - \frac{j}{Z_2 \tan \varphi_2} \\ y''_{12} &= \frac{y_{12}}{\cos \varphi_1 + j Z_1 \sin \varphi_1 \cdot y_{11}} + \frac{j}{Z_2 \sin \varphi_2} \\ y''_{21} &= \frac{y_{21}}{\cos \varphi_1 + j Z_1 \sin \varphi_1 \cdot y_{11}} + \frac{j}{Z_2 \sin \varphi_2} \\ y''_{22} &= y_{22} - \frac{j Z_2 \cdot \sin \varphi_1 \cdot y_{21} y_{12}}{\cos \varphi_1 + j Z_1 \sin \varphi_1 \cdot y_{11}} - \frac{j}{Z_2 \tan \varphi_2}. \end{aligned} \quad (13)$$

As a result, the parameter A'' of the entire DTL-feedback network can be expressed in (14), as shown at the bottom of this page, and to obtain a real value for A'' , the following relationship is required:

$$\begin{aligned} \frac{g_{21} Z_2 \sin \varphi_2 - g_{11} Z_1 \sin \varphi_1}{g_{12} Z_2 \sin \varphi_2 - g_{11} Z_1 \sin \varphi_1} &= A'' \\ \frac{b_{21} Z_2 \sin \varphi_2 - b_{11} Z_1 \sin \varphi_1 + \cos \varphi_1}{b_{12} Z_2 \sin \varphi_2 - b_{11} Z_1 \sin \varphi_1 + \cos \varphi_1} &= A''. \end{aligned} \quad (15)$$

Finally, (15) can be further transformed into the following conditions of transmission line parameters

(Z_1 , φ_1 , Z_2 , and φ_2):

$$Z_1 \cdot \tan \varphi_1 = \frac{1}{b_{11} - g_{11} \frac{A'' \cdot b_{12} - b_{21}}{A'' \cdot g_{12} - g_{21}}} \quad (16)$$

$$Z_2 \cdot \sin \varphi_2 = Z_1 \sin \varphi_1 \frac{A'' \cdot g_{11} - g_{11}}{A'' \cdot g_{12} - g_{21}} \quad (17)$$

where g_{ij} and b_{ij} are the real and imaginary parts of the Y -parameter of the original transistor [y_{ij} in (1)], and A'' is given in (6) for a certain G_{ma} .

Since $[Y_0]$ and U of an MOSFET can be obtained through a simple S-parameter simulation, our proposed DTL-network based on (16) and (17) offers an express and accurate way to achieve any desired $G_{ma} \in (0, G_{max})$. After DTL embedding, the combined network is unconditionally stable. Since G_{ma} and stability factor K have the following relationship [23]:

$$G_{ma} = |A''| (K - \sqrt{K^2 - 1}) \quad (18)$$

the value of K can be obtained by substituting (6) into (18)

$$K = 1 + \frac{(|\sqrt{G_{ma} U} - 1| - |\sqrt{G_{ma} U} - G_{ma}|)^2}{2|\sqrt{G_{ma} U} - G_{ma}| \cdot |\sqrt{G_{ma} U} - 1|}. \quad (19)$$

This design methodology has been verified through the simulations of a 65-nm NMOS transistor ($W_{gate} = 12 \mu\text{m}$) with an f_{max} of 250 GHz, and the results are plotted on a gain plane.² Various DTL-feedback structures with specified G_{ma} at 137.5 GHz are simulated, respectively. By gradually changing the transmission line parameters until they reach the calculated values given by (16) and (17), the movements of the U/A value are plotted in the gain plane shown in Fig. 9. Fig. 9(a) proves that with DTL feedback, various G_{ma} targets are achieved accurately. Fig. 9(b) shows that the proposed DTL feedback moves U/A to the real axis, achieving the largest distance from the stability boundary ($K = 1$) for a certain G_{ma} . Secondly, simulations are also performed at different frequency points (100, 137.5, 175, and 212.5 GHz) by setting $G_{ma} = G_{max}$, as shown in Fig. 10(a). The simulation shows that all designs land on the G_{max} curve as expected. At 137.5 GHz, G_{ma} is enhanced by 5 dB compared with the NMOS transistor without DTL network. To ensure adequate stability, our AMP design selects a G_{ma} slightly lower than G_{max} . For the 275-GHz AMP (with a 12- μm NMOS transistor pair and an input frequency of 137.5 GHz), the final DTL parameters are: $Z_1 = 30 \Omega$, $\theta_1 = 55^\circ$, $Z_2 = 80 \Omega$, and $\theta_2 = 88^\circ$. Through the tuning of θ_1 and θ_2 , the influence of DTL on the doubler efficiency can be verified in Fig. 10(b).

As shown in Fig. 11, while G_{ma} of the AMP approaches G_{max} using DTL feedback, the real part of the optimum

²On a gain plane, the real and imaginary parts of (U/A) for a network are used as the x - and y -values. Different G_{ma} values correlate to a set of circle contours and different K values correlate to a set of elliptical contours [20].

$$\begin{aligned} A'' &= \frac{y''_{21}}{y''_{12}} = \frac{y_{21} Z_2 \cdot \sin \varphi_2 - Z_1 \sin \varphi_1 y_{11} + j \cos \varphi_1}{y_{12} Z_2 \sin \varphi_2 - Z_1 \sin \varphi_1 y_{11} + j \cos \varphi_1} \\ &= \frac{(g_{21} Z_2 \sin \varphi_2 - g_{11} Z_1 \sin \varphi_1) + j (b_{21} Z_2 \sin \varphi_2 - b_{11} Z_1 \sin \varphi_1 + \cos \varphi_1)}{(g_{12} Z_2 \sin \varphi_2 - g_{11} Z_1 \sin \varphi_1) + j (b_{12} Z_2 \sin \varphi_2 - b_{11} Z_1 \sin \varphi_1 + \cos \varphi_1)} \end{aligned} \quad (14)$$

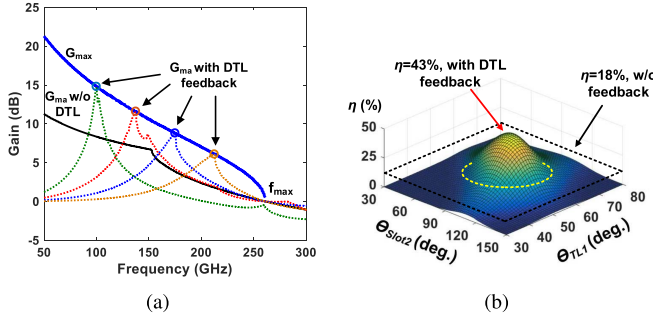


Fig. 10. (a) Simulated impedance-matched power gain of an MOS transistor with and without the DTL feedback. (b) Simulated doubler efficiency with and without DTL at 275 GHz.

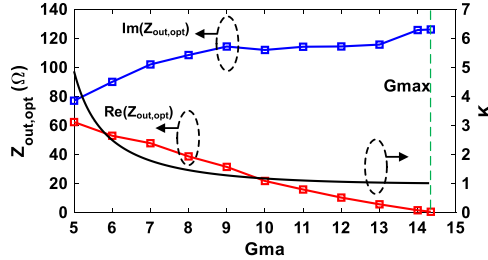


Fig. 11. Simulated optimum matched load impedance and stability factor for the 275-GHz AMP under different G_{ma} values (in a linear scale).

load impedance for conjugate impedance matching decreases, and its imaginary part increases. Thus, the output impedance matching of AMP needs a high quality factor resonator network. This is performed by *Slot 1*. The RF power from the drains is then injected into *Slot 1* and maximizes the output voltage swing. For the 275-GHz AMP, the optimum matched output impedance is $6 + j116 \Omega$ at $f_0 = 137.5$ GHz. A length of $185 \mu\text{m}$ is then selected for *Slot 1*, which maximizes the realized power gain, as shown in Fig. 12(a). For the 225-GHz AMP and 315-GHz AMP, which are at the two ends of the up-conversion and down-conversion chains, the lengths for *Slot 1* are 222 and $150 \mu\text{m}$, respectively. Their presented impedances at their channel center frequencies are $11 + j156 \Omega$ and $5 + j105 \Omega$, respectively. In addition, gain compression is also shown in Fig. 12(a) with slight change of the optimum length for *Slot 1*. Fig. 12(b) shows that the doubler efficiency under RF driving power of 3 dBm at f_0 also peaks at $185 \mu\text{m}$ due to the nonlinearity generated by strong voltage swing of fundamental signal. Finally, it should also be noticed that the length of *Slot 1* ($185 \mu\text{m}$) is only slightly smaller than $\lambda/4 = 227 \mu\text{m}$ at f_0 and $\lambda/2 = 214 \mu\text{m}$ at $2f_0$ according to Fig. 6.

C. Even-Mode Operation at the Second-Harmonic Frequency $2f_0$

The second-harmonic signal generated from the MOSFET drain nodes is in common mode. Accordingly, the signal flow inside the AMP core is shown in Fig. 13(a). The distribution of its electrical field is presented in Fig. 7(b). The following three points are worth mentioning.

- 1) The folded *Slot 1*, previously used for output impedance matching at f_0 , now becomes nearly quarter-wavelength

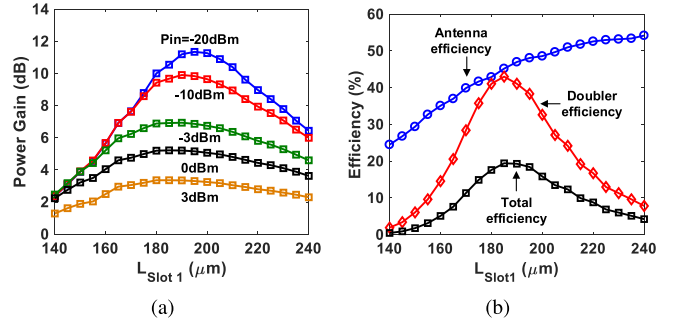


Fig. 12. (a) Simulated realized power gain of the AMP at 275 GHz versus the length of *Slot 1*. (b) Simulated antenna efficiency, doubler efficiency, and total efficiency of the AMP at 275 GHz with various lengths of *Slot 1*.

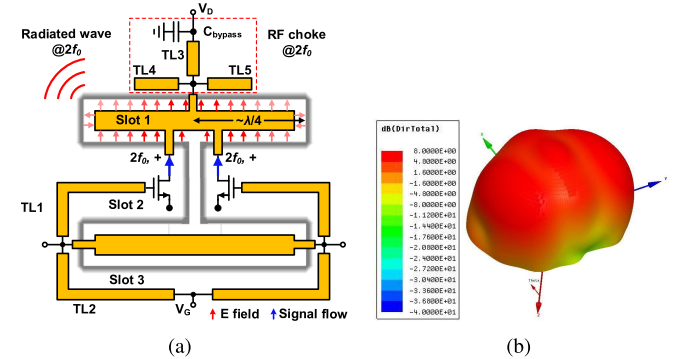


Fig. 13. (a) Even-mode signal flow of the AMP at the second-harmonic frequency $2f_0$. (b) Simulated radiation pattern of the AMP.

for each of its folded section. Four in-phase standing waves are then formed inside, and *Slot 1* acts as a folded slot antenna with backside radiation. In a full-wave electromagnetic simulation using ANSYS HFSS [24], assuming semi-infinite silicon in the chip back to emulate a hemispheric silicon lens in practice, the simulated radiation directivity and efficiency of the 275-GHz AMP are 8 dBi [Fig. 13(b)] and 45% [Fig. 12(b)], respectively.

- 2) No harmonic wave at $2f_0$ exists inside the vertical portion of *Slot 2*. This is because a slot transmission line presents a very high cutoff frequency for a common-mode signal that is associated with a TM wave. This means that although *Slot 2* behaves as a feedback path for the fundamental signal at f_0 , it eliminates the leakage of the generated signal at $2f_0$ to the lossy input gates. Such signal filter, implemented in a very short slot line, provides broad bandwidth and low insertion loss.
- 3) The output impedance matching for the second harmonic signal on the drain is partly performed by the microstrip lines within the RF choke shown in Fig. 13(a). For the 275-GHz AMP, the impedance of the slot antenna is $49 + j41 \Omega$, which matches well with the impedance presented by the drain ($43-j23 \Omega$). A metal-to-metal capacitor C_{bypass} of 150 fF provides a bypass path for the $2f_0$ signal and reflects its power back to AMP; meanwhile, the RF choke does not affect the differential signal at f_0 , since a virtual ground is formed at the

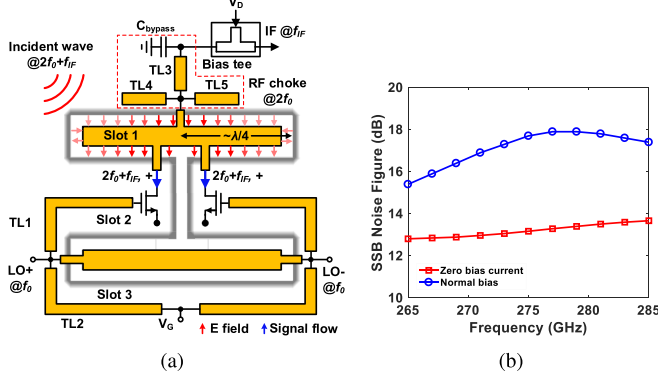


Fig. 14. (a) Sub-harmonic mode operation and IF extraction. (b) Simulated SSB-NF of the AMP.

junction of TL 3, TL 4, and TL 5 [Fig. 13(a)] at this frequency.

Utilizing the orthogonality of electromagnetic modes and the geometric manipulation of standing-wave patterns, *Slot 1* and *Slot 2* are multi-functional at f_0 and $2f_0$. Such design methodology, therefore, effectively reduces passive loss. Similar approaches were also shown in [19] and [25]. In simulation, each AMP consumes about 30 mW of dc power and the doubler conversion efficiency at 275 GHz before on-chip radiation is 43%, as shown in Fig. 10(b). It is noteworthy that compared with conventional topology without using the DTL feedback, the conversion efficiency is improved by $2.4 \times$. As shown in Fig. 12(b), although the antenna efficiency is reduced by $\sim 10\%$ because the length of *Slot 1* is slightly smaller than the ideal value of $\lambda/2$ at $2f_0$ (Section III-B), the total efficiency, including the on-chip radiation, still reaches 19%.

D. Receiver Mode for the Input Radiation Near $2f_0$

We note that *Slot 1* is a reciprocal component. In the receiver mixer mode, as shown in Fig. 14(a), input wave at $2f_0 + f_{IF}$ is coupled through *Slot 1* (with the same 45% coupling efficiency) into the heavily driven transistor pair, where the input wave is mixed with the locally generated signal at $2f_0$. Since both of these signals are in common mode, the down-converted f_{IF} signals from the two transistors are in phase and are then combined and extracted from the top of the AMP structure through an integrated RF chock at $2f_0$ and an off chip bias tee.

The simulated SSB NF, excluding antenna loss, is 17.7 dB at 275 GHz [Fig. 14(b)]. It is further improved to 13.2 dB when the transistor bias current is zero (hence varistor-mode mixer) due to lower thermal and flicker noise.

IV. DESIGN OF OTHER CIRCUIT BLOCKS

A. Mode-Filtering-Based THz Slot Balun

As indicated in Fig. 2(a), inside each AMP, the differential input signal at fundamental frequency f_0 is provided by a balun. On the other hand, however, any phase and amplitude imbalance from the balun does not only deteriorate the AMP

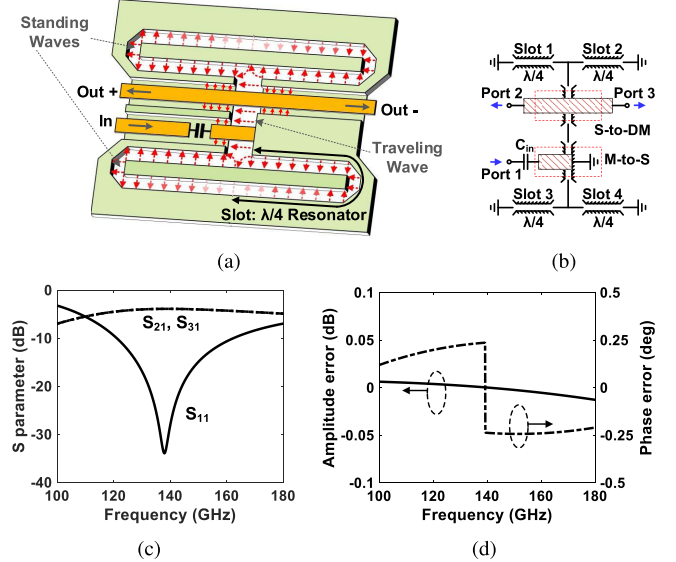


Fig. 15. Slot balun design. (a) Physical structure and electrical-field distribution. (b) Schematic. (c) Simulated S-parameters. (d) Simulated output amplitude and phase errors.

doubler efficiency, but also causes radiation leakage at f_0 . To eliminate such signal imbalance, a new on-chip balun structure based on orthogonal-mode filtering is developed. Its 3-D structure and circuit schematic are presented in Fig. 15(a) and (b), respectively. The balun consists of a microstrip-to-slot (M-to-S) transition at the input and a slot-to-differential-microstrip transition (S-to-DM) at the output. The two parts are connected through a short vertical slot line. Similar to the harmonic isolation method in the AMP, when the input signal is coupled into the vertical slot line through the M-to-S transition, only the odd-mode TE wave propagates along the slot. The even-mode TM wave signal is suppressed. Next, we note that the top S-to-DM transition is fully symmetric. Thus, when it is fed by the odd-mode-only TE wave through the vertical slot in the center, the two output signals are completely differential. In contrast to the vertical slot containing traveling TE wave, *Slot 1* ~ *Slot 4* in Fig. 15(b) contain only standing waves; their role is to enclose the vertical slot with a high impedance for wave confinement.

Different from other conventional baluns (e.g., Marchand balun), which by principle requires each branch to be quarter-wavelength in order to achieve perfect output balance at only one frequency point, our balun filters out the undesired output common mode over the entire operation bandwidth. The simulated S-parameters of the balun, presented in Fig. 15(c), indicate broadband matching and a minimum insertion loss ($|S_{21,31}| - 3\text{dB}$) of only 0.9 dB. The simulated amplitude ($\sim 0.02 \text{ dB}$) and phase errors ($\sim 0.25^\circ$) across 80-GHz bandwidth, shown in Fig. 15(d), are nearly negligible; it is suspected that such errors stem from the asymmetric input structure and limited simulation precision.

B. Up-/Down-Conversion Frequency Mixer

The frequency mixers used in both the up-conversion and down-conversion chains (with a conversion step of 5 GHz)

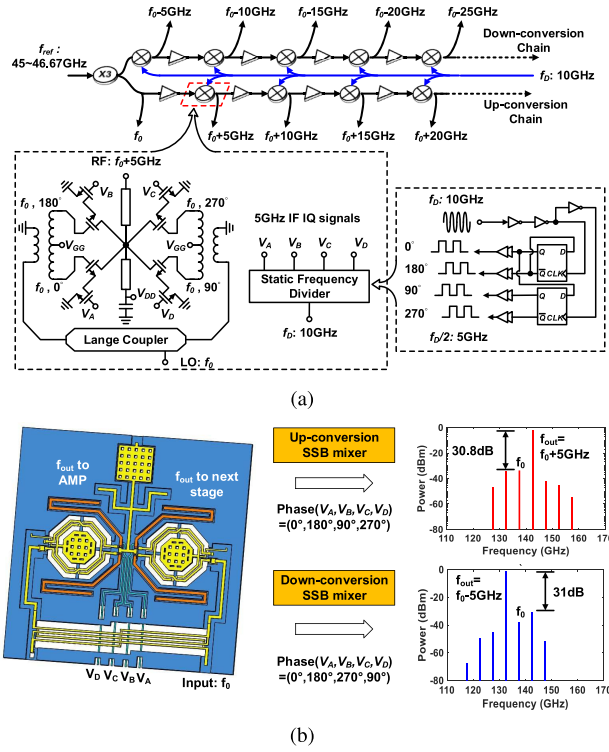


Fig. 16. (a) Schematic and (b) 3-D view and simulated output spectra of the SSB up-/down-conversion mixers.

of the comb adopt a multi-phase mixer design. As shown in Fig. 16(a), four cascode MOSFETs are connected together at their drains, which are driven by RF ($f_0 = 110 \sim 160\text{ GHz}$) and IF ($V_A \sim V_D$) signals with quadrature phases. Different branches mix the RF and IF signals with different combinations of the I/Q phases. At the central output node, the mixed signals are combined in current mode, which leads to: 1) the generation of an SSB output signal and 2) the cancellation of the unwanted harmonic signals. Inside each branch, the bottom transistor, driven by the 5-GHz IF signal, has a switching behavior and periodically turns the top transistor into saturation and cutoff modes. This configuration, being a special case of Gilbert mixer [26], is selected because at THz frequency, the switched-ON MOSFET, if placed at the output side, presents a severe power leakage path through its gate capacitance and increases mixer conversion loss.

The up- or down-conversion function in each mixer is selected by the connections of the quadrature IF signals ($V_A \sim V_D$) at 5 GHz [Fig. 16(b)], which are generated by a static divided-by-2 digital counter built inside each mixer [Fig. 16(a)]. The quadrature RF signals at f_0 are generated by two Lange couplers. In simulation, the mixer consumes a dc power of 19 mW, and achieves a conversion loss of 2.3 dB and an LO/image rejection of 30 dB [Fig. 16(b)]. In each frequency-conversion chain, the mixer loss is compensated by inter-stage amplifiers [Fig. 16(a)].

C. 135-GHz Input Frequency Tripler

In order to lower the external input frequency required to feed into the chip, a frequency tripler that generates a signal

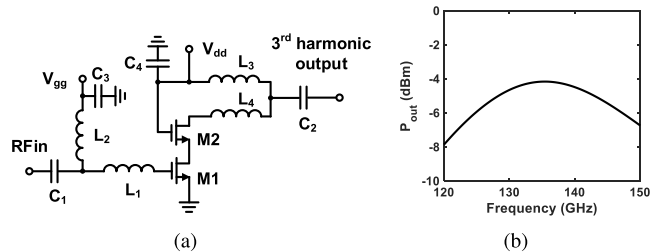


Fig. 17. (a) Schematic and (b) simulated output power of the 135-GHz input frequency tripler ($P_{in} = 6\text{ dBm}$).

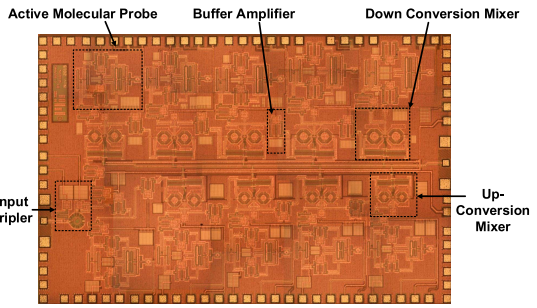


Fig. 18. Micrograph of the CMOS frequency-comb spectrometer (die size: $3 \times 2\text{ mm}^2$).

at 135–140 GHz is implemented. As shown in Fig. 17(a), the tripler is based on a cascode topology with input and output matching networks tuned at the fundamental ($\sim 45\text{ GHz}$) and third-harmonic ($\sim 135\text{ GHz}$) frequencies, respectively. The bottom transistor operates in Class-AB mode for maximum nonlinearity. With an input power of 6 dBm, the simulated output power of the tripler is plotted in Fig. 17(b). The tripler consumes 32 mW of dc power.

V. EXPERIMENTAL RESULTS

A. Chip Prototype and Characterizations

The spectrometer is implemented using TSMC bulk 65-nm CMOS process ($f_{max} = 250\text{ GHz}$). Fig. 18 shows the micrograph of the chip, which occupies an area of $3 \times 2\text{ mm}^2$. To facilitate the backside radiation, the chip is glued onto a high-resistivity silicon wafer (thickness = $250\text{ }\mu\text{m}$) first, and then a high-resistivity silicon lens (with 1 cm diameter) is attached on the backside of it. Compared with hyperhemispheric lens, hemispheric lens, although not providing additional beam collimation, has smaller sensitivity to the position offset of on-chip antennas from the chip center.

Each AMP on the chip can be turned on and off using its own power supply bias. This enables independent characterization for the radiation of each individual comb line. First, at a far-field distance of 10 cm, the AMP radiation pattern and spectrum are measured using a WR-3.4 Virginia Diode even-harmonic mixer (EHM) and a horn antenna (Fig. 19). A typical antenna pattern, measured from the AMP at 265 GHz, is shown in Fig. 20. The average measured directivity of the ten AMPs is 10.1 dBi, which is higher than the simulation results (8 dBi) reported in Section III-C. This is because the thickness of the chip ($150\text{ }\mu\text{m}$) and the silicon wafer introduces

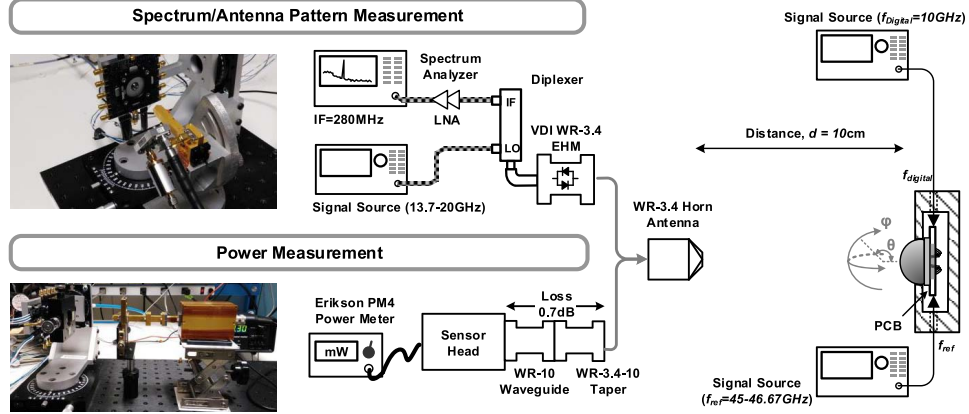


Fig. 19. Experimental setup for the characterization of spectrum, radiation pattern, and radiated power.

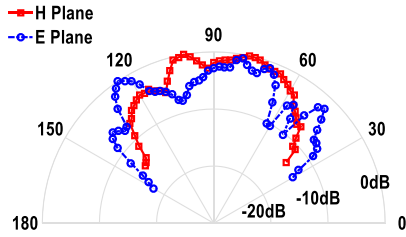


Fig. 20. Measured radiation pattern of one output channel (265 GHz).

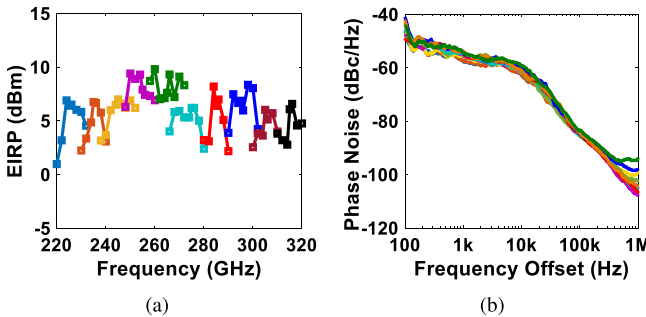


Fig. 21. Measured (a) EIRP and (b) phase noise of the frequency-comb line output (represented by different colors).

a small displacement of the on-chip antennas from the center of the hemispheric silicon lens [27].

Next, Fig. 21(b) shows the phase noise of the ten comb lines, with an average value of -102 dBc/Hz at 1-MHz offset. They are measured from the 280-MHz IF signal of EHM. The EHM LO, generated from an HP 83732B signal source, has a phase noise of -130 dBc/Hz at 1-MHz offset; therefore, the EHM has an intrinsic phase noise of $-130 \text{ dBc/Hz} + 20\log_{10}(16) = -106 \text{ dBc/Hz}$ at 1-MHz offset due to its 16th-harmonic mixing. Meanwhile, the phase noise of the $45 \sim 46.67 \text{ GHz}$ chip input, from a Keysight E8257D signal source, is also -130 dBc/Hz at 1-MHz offset, corresponding to a phase noise of -114 dBc/Hz at the chip output due to the on-chip multiplication factor of 6. Finally, the phase noise of the 10-GHz digital signal input of the chip (from Keysight N5173B signal generator) is -128 dBc/Hz at 1-MHz offset.

In conclusion, the reported phase noise in Fig. 21(b) should be dominated by the EHM intrinsic noise; and the actual phase noise of the chip radiation should be better.

To characterize the radiated power level, an Erikson PM4 absolute power meter is used (Fig. 19). Any possible radiation at the fundamental frequencies of the chip is completely filtered out by the input WR-3.4 horn antenna and waveguide. The measured equivalent isotropically radiated power (EIRP) of each comb line, with the comb input frequency [f_{ref} in Fig. 2(a)] sweeping from 45 to 46.67 GHz, is shown in Fig. 21(a). The entire 220–320 GHz band is seamlessly covered. Based on the measured antenna directivity (Fig. 20) and EIRP [Fig. 21(a)], the radiated power (without the beam collimation effect) of individual each comb line ranges from 0.23 to 0.88 mW. The total radiated power of the ten comb lines is 5.2 mW. We also rotate the chip by 90° so that the polarization of the radiated THz wave is orthogonal to that of the horn antenna. Under such a condition, the reading of the PM4 power meter drops to near zero, verifying that the previously measured power does not include the thermal radiation. It is noteworthy that, for a fixed total scanning time (integration time per data point \times number of data points), dual-THz-comb architecture enables $20\times$ longer integration time per point, when compared with a single-tone spectrometer. Thus, even if the radiated power of a single comb line is $20\times$ lower than that of a single-tone spectrometer, the SNR still does not deteriorate. Therefore, it is the total radiated power of the comb, rather than simply the power of each comb line, that determines the spectrometer performance.

To characterize the receiver mode of the comb spectrometer, an OML WR-3.4 network analyzer frequency extender is used as a tunable source at $220 \sim 320 \text{ GHz}$ (Fig. 22). Prior to the chip measurement, the output power of the frequency extender P_{TX} at each frequency point is calibrated. Next, the SSB conversion gain G_{conv} of each AMP receiver, defined as the following expression, is measured:

$$G_{\text{conv}}|_{\text{dB}} = P_{\text{IF,out}}|_{\text{dBm}} - P_{R,\text{ant}}|_{\text{dBm}} \quad (20)$$

where $P_{\text{IF,out}}$ is the output power from the IF port of each AMP and $P_{R,\text{ant}}$ is the THz power received by each AMP

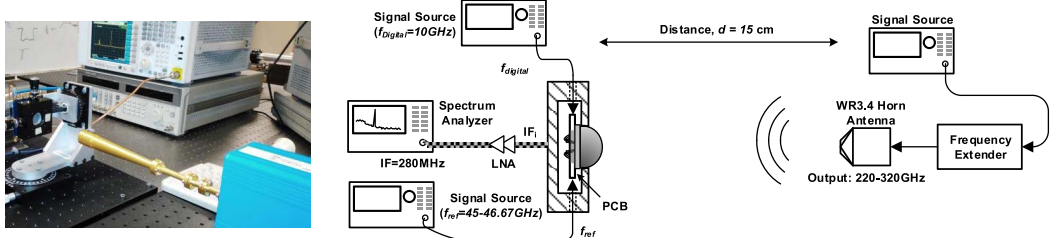


Fig. 22. Experimental setup for the characterizations of conversion gain and NF.

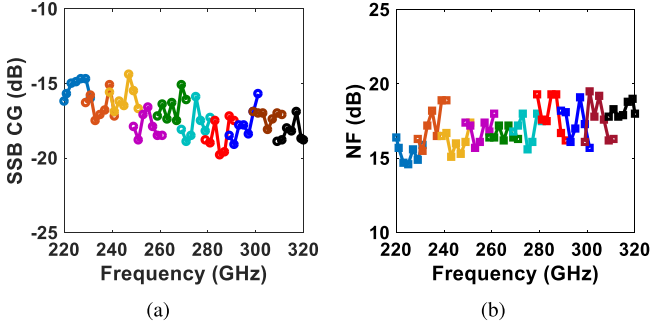


Fig. 23. (a) Measured SSB conversion gain and (b) measured SSB NF of each frequency-comb channel.

antenna aperture, which is obtained by

$$\begin{aligned} P_{R,\text{ant}}|\text{dBm} &= P_{\text{TX}}|\text{dBm} + G_{\text{TX,ant}}|\text{dBi} \\ &\quad - L_{\text{path}}|\text{dB} + D_{\text{RX,ant}}|\text{dBi}. \end{aligned} \quad (21)$$

In (21), $G_{\text{TX,ant}}$ is the gain of the source horn antenna (~ 25 dBi), L_{path} is the path loss at distance of 15 cm, and $D_{\text{RX,ant}}$ is the previously measured AMP radiation directivity. As a result, our measured conversion gain [shown in Fig. 23(a)] *includes* the loss of the on-chip antenna but *de-embeds* the gain factor provided by the beam collimation. Finally, the noise floor $P_{n,\text{out}}$ (dBm/Hz) at each IF output port is also measured and used in the calculation of the SSB NF

$$\text{NF}|\text{dB} = P_{n,\text{out}}|\text{dBm}/\text{Hz} - (-174\text{dBm}/\text{Hz}) - G_{\text{conv}}|\text{dB}. \quad (22)$$

Fig. 23(b) presents the final measured SSB NF (including antenna loss) of the spectrometer, which ranges from 14.6 to 19.5 dB within 220–320 GHz band.

The chip consumes a dc power of 1.7 W, resulting in an energy efficiency of 0.17 mJ/point (1-ms integration time) in spectral sampling. The ten AMPS consume a dc power of 287 mW, which corresponds a dc-to-THz efficiency of 1.8%; 1.177 W of the total dc power is consumed by 41 inter-stage buffer amplifiers. The up-/down-conversion mixers (including static frequency divider) consume 199 mW. The input tripler consumes 32 mW. The overall dc-to-THz efficiency is 0.3%.

B. THz Spectroscopy Demonstration

A spectroscopy setup with the CMOS comb spectrometer as the broadband signal source and detector has been established [Fig. 24(a)]. It is improved based on the experimental

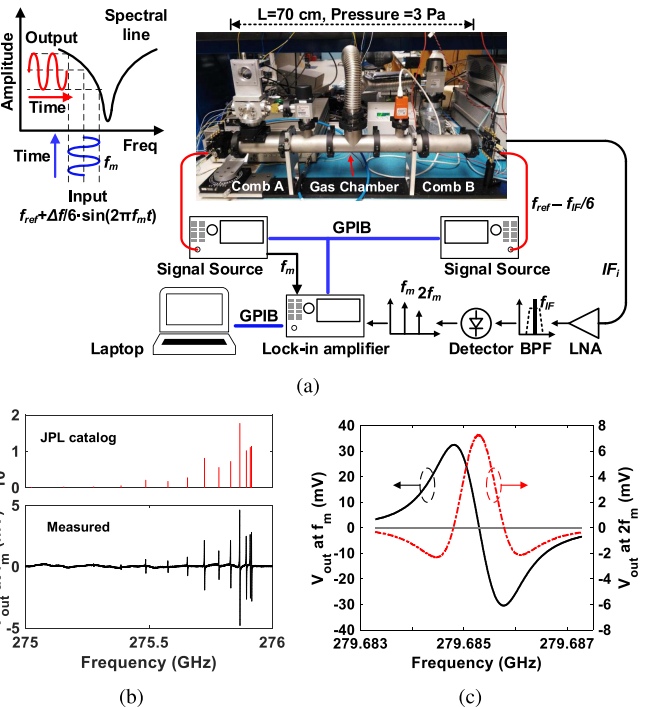


Fig. 24. (a) Experimental setup of the THz rotational spectroscopy using the CMOS dual-comb chipset. (b) Section of measured absorption spectrum of acetonitrile (CH_3CN). (c) Measured spectral line of OCS using wavelength modulation with $f_m = 50$ kHz. [Note: LGINT in (b) refers to the integrated line intensity in log scale from the JPL catalog.]

system of [14]. A passive IF square-law rectifier (Crystek CPDETLS-4000) replaces the detector with a built-in amplifier in the previous system, which significantly reduces the detector noise and the voltage ripple due to dc power supply. In our measurement, periodic standing-wave pattern in the direct transmission/sweeping mode is observed because of the undesired wave reflection at the gas cell windows. Such a pattern tilts the baseline and causes asymmetry of the measured spectral curve. To reduce such effects, wavelength modulation of the THz signal with a modulation frequency f_m of 50 kHz and a frequency deviation Δf of 240 kHz is applied to the chip. Therefore, the output signals of the off-chip detector [Fig. 24(a)] at f_m and $2f_m$ correspond to only the first- and second-derivatives of the gas spectral line. This significantly reduces the slow-varying spectral baseline.

Using a molecular turbo pump, a gas sample of acetonitrile (CH_3CN) with a pressure of 3 Pa is injected into a tube with a signal propagation path length of 0.7 m. Measured at f_m , one spectral section of the molecule absorption from

TABLE I
PERFORMANCE COMPARISON OF THz SOURCES IN SILICON

Ref.	Technology (f_{max})	Circuit Type	Frequency (GHz)	Bandwidth (GHz)	Total Radiated Power (mW)	Phase Noise ($\Delta f=1$ MHz) (dBc/Hz)	Noise Figure (dB)	DC Power (W)	Chip Area (mm ²)
[11]	130-nm SiGe (500 GHz)	Single Tone (TX+RX)	245	14	4	-85	18	1.5+0.6 (TX+RX)	20
[12]	65-nm CMOS	Single Tone (TX+RX)	208~255	47	0.1 ¹	-80	N/A	1.4	5.6
[13]	65-nm CMOS	Single Tone (RX)	210~305	95	N/A	N/A	18.4~23.5 ²	N/A	1.3
[29]	32-nm CMOS (320 GHz)	Transceiver (TX+RX)	210	14	0.7 ³	-81	11~12 ⁴	0.24+0.086 (TX+RX)	4.6
[30]	45-nm CMOS	Transceiver (TX+RX)	90-300	210	0.12	N/A	29~37	0.065+0.036 (TX+RX)	2.98
This Work	65-nm CMOS (250 GHz)	Comb (TX+RX)	220~320	100	5.2 ⁵	-102 ⁶	14.6-19.5	1.7	6

¹ The reported power is EIRP, which includes the antenna gain of the chip.

² The NF is derived from the reported isotropic noise figure (13.9~19 dB), which includes the improvement due to the antenna gain, minus the reported antenna directivity (3~5 dBi).

³ The radiated power is estimated from the PA output power of 2.9 mW and the antenna loss of 6 dB.

⁴ The NF of the low-noise amplifier is used here without including the on-chip antenna loss of 6 dB.

⁵ Total radiated power of 10 comb lines. A silicon lens with a diameter of 1 cm is used for backside radiation.

⁶ An external signal generator (Keysight E8257D) is used rather than on-chip VCOs used in [11], [12], [29]. Details of phase noise analysis is presented at Section V-A.

275 to 276 GHz is shown in Fig. 24(b). The location of spectral lines and relative line intensity agrees well with the JPL molecular spectroscopy catalog [3]. In addition, Fig. 24(c) presents a single absorption line of OCS at 279.685 GHz under 3-Pa pressure using the identical experiment setup. The results at f_m and $2f_m$ are presented. The effective noise bandwidth of the lock-in amplifier is 7.8 Hz, and the noise floor of the entire system is measured as $17 \mu V/\sqrt{Hz}$.

Under Doppler-limited condition, the measured full line width at half maximum in Fig. 24(c) is 590 kHz for the $2f_m$ measurement, which is associated with a quality factor of 4.7×10^5 . This not only demonstrates the absolute detection specificity, but also clearly shows the necessity of 10-kHz level scanning resolution, which is only achievable using a CW scheme. The highest SNR for CH₃CN in the f_m measurement with 1-Hz bandwidth [Fig. 24(b)] is 49 dB. The SNRs for OCS obtained in Fig. 24(c) are 66 and 53 dB at f_m and $2f_m$, respectively, with 1-Hz bandwidth. It should be noticed that further SNR enhancement can be achieved by beam collimation using external THz lenses [28].

Since our CMOS spectrometer fully covers a broad frequency range of 220–320 GHz, it is capable of analyzing gas mixture with almost any polar molecules heavier than HCN. The spectroscopic demonstration is performed channel by channel separately due to the limitation of instruments. For each IF channel under testing, identical hardware of signal processing is used, including an IF LNA, a bandpass filter, an envelope detector, and a lock-in amplifier. This paper demonstrates only the THz front end of the proposed architecture [Fig. 1(b)], which is the key enabling technology. We expect that using this technology, future on-chip spectrometer can achieve true simultaneous multi-channel operation by integrating lock-in amplifier circuitry to each channel. Since the lock-in amplifier circuitry, essentially a low-frequency (~50 kHz) heterodyne receiver plus an integrator, has low-power consumption, it should not deteriorate the overall performance of the chip.

VI. CONCLUSION

The wide bandwidth of THz waves presents both new opportunities in applications and challenges in electronic designs. In this paper, we demonstrate significant speed and efficiency improvement using a highly parallel architecture. This approach leverages the large integration capability offered by silicon integrated circuits, while not significantly increasing chip area, thanks to the small wavelength and component size. It is worth mentioning that operations with parallelism enhance the efficiencies of not only the THz front ends but also the peripheral supporting circuitries. For example, although our spectrometer covers a fractional bandwidth of 37%, the required tuning range of the millimeter-wave frequency synthesizer for the chip input (f_{ref} in Fig. 2) is only 3.7%. Additionally, the run time of this synthesizer is greatly reduced (> 20×). These two factors lead to significant extra energy saving.

In addition, we also present a design methodology that utilizes versatile electromagnetic structures to optimize solid-state device operations at multiple frequencies. Although THz electronics are strongly limited by the device speed, there is still big room for efficiency improvement, when a single THz circuit is designed to be multi-functional. Table I shows a comparison between this paper and other state-of-the-art systems implemented in silicon and operating above 200 GHz. The total radiated power and sensitivity demonstrated by our spectrometer are so far the highest in silicon-based THz circuits.

ACKNOWLEDGMENT

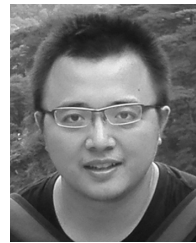
The authors would like to thank Dr. S. Coy, Prof. R. Field, Prof. K. Nelson (Chemistry Department, MIT), Prof. J. Muentner (Chemistry Department, University of Rochester), Dr. B. Perkins (MIT Lincoln Laboratories), and Prof. Q. Hu (EECS Department, MIT) for technical discussions. They would like to thank Dr. R. Temkin (Physics Department, MIT), Prof. E. Afshari (EECS Department, University of Michigan), Prof. A. Chandrakasan, and Prof. T. Palacios (EECS Department, MIT) for their support of testing

instruments. They would also like to thank T. Shi and Z. Wang (Fudan University and MIT) for their technical assistance.

The chip fabrication of this paper is provided by the TSMC University Shuttle Program.

REFERENCES

- [1] I. R. Medvedev, C. F. Neese, G. M. Plummer, and F. C. De Lucia, "Sub-millimeter spectroscopy for chemical analysis with absolute specificity," *Opt. Lett.*, vol. 35, no. 10, pp. 1533–1535, 2010.
- [2] C. H. Townes and A. L. Schawlow, *Microwave Spectroscopy* (Dover Books on Physics), 2nd ed. Mineola, NY, USA: Dover Publications, Inc., 2012.
- [3] Jet Propulsion Laboratory, *Molecular Spectroscopy Catalog*. Accessed: Apr. 30, 2017. [Online]. Available: <https://spec.jpl.nasa.gov/>
- [4] C. F. Neese, I. R. Medvedev, G. M. Plummer, A. J. Frank, C. D. Ball, and F. C. De Lucia, "Compact submillimeter/terahertz gas sensor with efficient gas collection, preconcentration, and ppt sensitivity," *IEEE Sensors J.*, vol. 12, no. 8, pp. 2565–2574, Aug. 2012.
- [5] R. Han *et al.*, "On-chip terahertz electronics: From device-electromagnetic integration to energy-efficient, large-scale microsystems," in *IEDM Tech. Dig.*, San Francisco, CA, USA, Dec. 2016, pp. 29.6.1–29.6.4.
- [6] Z. Ahmad *et al.*, "Devices and circuits in CMOS for THz applications," in *IEDM Tech. Dig.*, San Francisco, CA, USA, Dec. 2016, pp. 29.8.1–29.8.4.
- [7] M. M. Assefzadeh and A. Babakhani, "Broadband THz spectroscopic imaging based on a fully-integrated 4 × 2 digital-to-impulse radiating array with a full-spectrum of 0.03–1.03 THz in silicon," in *Proc. IEEE Symp. VLSI Circuits (VLSIC)*, Jun. 2016, pp. 1–4.
- [8] X. Wu and K. Sengupta, "Programmable picosecond pulse generator in CMOS," in *IEEE MTT-S Int. Microw. Symp. Dig.*, May 2015, pp. 1–4.
- [9] R. Han and E. Afshari, "A CMOS high-power broadband 260-GHz radiator array for spectroscopy," *IEEE J. Solid-State Circuits*, vol. 48, no. 12, pp. 3090–3104, Dec. 2013.
- [10] X. Wu and K. Sengupta, "A 40-to-330 GHz synthesizer-free THz spectroscope-on-chip exploiting electromagnetic scattering," in *IEEE Int. Solid-State Circuits Conf. (ISSCC) Dig. Tech. Papers*, Jun. 2016, pp. 428–429.
- [11] K. Schmalz *et al.*, "245-GHz transmitter array in SiGe BiCMOS for gas spectroscopy," *IEEE Trans. THz Sci. Technol.*, vol. 6, no. 2, pp. 318–327, Mar. 2016.
- [12] N. Sharma *et al.*, "200–280 GHz CMOS RF front-end of transmitter for rotational spectroscopy," in *Proc. IEEE Symp. VLSI Technol.*, Jun. 2016, pp. 1–2.
- [13] Q. Zhong, W. Choi, C. Miller, R. Henderson, and K. O. Kenneth, "A 210-to-305 GHz CMOS receiver for rotational spectroscopy," in *IEEE Int. Solid-State Circuits Conf. (ISSCC) Dig. Tech. Papers*, vol. 3, Jan. 2016, pp. 426–427.
- [14] C. Wang and R. Han, "Rapid and energy-efficient molecular sensing using dual mm-Wave combs in 65 nm CMOS: A 220-to-320 GHz spectrometer with 5.2 mW radiated power and 14.6-to-19.5 dB noise figure," in *IEEE Int. Solid-State Circuit Conf. (ISSCC) Dig. Tech. Papers*, San Francisco, CA, USA, Feb. 2017, pp. 18–20.
- [15] J. Ko and R. Gharpurey, "A pulsed UWB transceiver in 65 nm CMOS with four-element beamforming for 1 Gbps meter-range WPAN applications," *IEEE J. Solid-State Circuits*, vol. 51, no. 5, pp. 1177–1187, May 2016.
- [16] A. Medi and W. Namgoong, "A high data-rate energy-efficient interference-tolerant fully integrated CMOS frequency channelized UWB transceiver for impulse radio," *IEEE J. Solid-State Circuits*, vol. 43, no. 4, pp. 974–980, Apr. 2008.
- [17] Y.-D. Hsieh *et al.*, "Terahertz comb spectroscopy traceable to microwave frequency standard," *IEEE Trans. THz Sci. Technol.*, vol. 3, no. 3, pp. 322–330, May 2013.
- [18] D. Burghoff *et al.*, "Terahertz laser frequency combs," *Nature Photon.*, vol. 8, no. 6, pp. 462–467, 2014.
- [19] R. Han *et al.*, "A SiGe terahertz heterodyne imaging transmitter with 3.3 mW radiated power and fully-integrated phase-locked loop," *IEEE J. Solid-State Circuits*, vol. 50, no. 12, pp. 2935–2947, Dec. 2015.
- [20] R. Spence, *Linear Active Networks*. Hoboken, NJ, USA: Wiley, 1970.
- [21] Z. Wang and P. Heydari, "A study of operating condition and design methods to achieve the upper limit of power gain in amplifiers at near- f_{max} frequencies," *IEEE Trans. Circuits Syst. I, Reg. Papers*, vol. 64, no. 2, pp. 261–271, Feb. 2017.
- [22] H. Bameri and O. Momeni, "A high-gain mm-wave amplifier design: An analytical approach to power gain boosting," *IEEE J. Solid-State Circuits*, vol. 52, no. 2, pp. 357–370, Feb. 2017.
- [23] D. M. Pozar, *Microwave Engineering*, 4th ed. Hoboken, NJ, USA: Wiley, 2011.
- [24] *User's Guide—High Frequency Structure Simulator*, ANSYS Inc., Canonsburg, PA, USA, 2014.
- [25] K. Sengupta and A. Hajimiri, "Distributed active radiation for THz signal generation," in *IEEE Int. Solid-State Circuits Conf. (ISSCC) Dig. Tech. Papers*, Feb. 2011, pp. 288–289.
- [26] K. H. Clarke and D. T. Hess, *Communication Circuits: Analysis and Design* (Addison-Wesley Series in Electrical Engineering). Reading, MA, USA: Addison-Wesley, 1971.
- [27] D. B. Rutledge, D. P. Neikirk, and D. P. Kasilingam, "Integrated-circuit antennas," in *Infrared and Millimeter Waves*, vol. 10. Orlando, FL, USA: Academic, 1983, pp. 1–90.
- [28] C. Wang, B. Perkins, Z. Wang and R. Han, "Molecular detection for unconcentrated gas with ppm sensitivity using 220-to-320 GHz dual-frequency-comb spectrometer in CMOS," *IEEE Trans. Biomed. Circuits Syst.*, to be published.
- [29] Z. Wang, P.-Y. Chiang, P. Nazari, C.-C. Wang, Z. Chen, and P. Heydari, "A CMOS 210-GHz fundamental transceiver with OOK modulation," *IEEE J. Solid-State Circuits*, vol. 49, no. 3, pp. 564–580, Mar. 2014.
- [30] T. Chi, M.-Y. Huang, S. Li, and H. Wang, "A packaged 90-to-300 GHz transmitter and 115-to-325 GHz coherent receiver in CMOS for full-band continuous-wave mm-wave hyperspectral imaging," in *IEEE Int. Solid-State Circuits Conf. (ISSCC) Dig. Tech. Papers*, Feb. 2017, pp. 304–305.



Cheng Wang (S'15) was born in Suining, China, in 1987. He received the B.S. degree in engineering physics from Tsinghua University, Beijing, China, in 2008, and the M.S. degree in radio physics from the China Academy of Engineering Physics, Mianyang, China, in 2011. He is currently pursuing the Ph.D. degree with the Department of Electrical Engineering and Computer Science, Massachusetts Institute of Technology, Cambridge, MA, USA.

From 2011 to 2015, he was with the Institute of Electronic Engineering, Mianyang, as an Assistant Research Fellow. His current research interests include millimeter/terahertz-wave gas spectroscopy, high-precision clock generation, broadband communication, and radar imaging.

Mr. Wang received the Analog Device Inc. Outstanding Student Designer Award in 2016 and the IEEE Microwave Theory and Techniques Society Boston Chapter Scholarship in 2017.



Ruonan Han (S'10–M'14) received the B.Sc. degree in microelectronics from Fudan University, Shanghai, China, in 2007, the M.Sc. degree in electrical engineering from the University of Florida, Gainesville, FL, USA, in 2009, and the Ph.D. degree in electrical and computer engineering from Cornell University, Ithaca, NY, USA, in 2014.

In 2012, he was an Intern with Rambus Inc., Sunnyvale, CA, USA, designing energy-efficient I/O circuits. He is currently an Assistant Professor with the Department of Electrical Engineering and Computer Science, Massachusetts Institute of Technology, Cambridge, MA, USA. His current research interests include microelectronic circuits and systems operating at millimeter-wave and terahertz frequencies for novel sensing and ultrahigh-speed communications.

Dr. Han is a member of the IEEE Solid-State Circuits Society and the IEEE Microwave Theory and Techniques Society. He was a recipient of the Cornell ECE Directors Ph.D. Thesis Research Award, the Cornell ECE Innovation Award, two best student paper awards of the IEEE Radio-Frequency Integrated Circuits Symposium in 2012 and 2017, the Irwin and Joan Jacobs Fellowship, the John M. Olin Fellowship, the IEEE Microwave Theory and Technique Society Graduate Fellowship Award, the IEEE Solid-State Circuits Society Predoctoral Achievement Award, and the National Science Foundation CAREER Award in 2017. He currently holds the MIT E. E. Landsman (1958) Career Development Chair Professorship.